

Electronic Supplementary Information for **High Performance Aluminum-Cerium Alloys for High- Temperature Applications**

Zachary C. Sims, Orlando R. Rios, David Weiss, Patrice E. A. Turchi, Aurelien Perron, Jonathan R. I. Lee, Tian T. Li, Joshua A. Hammons, Michael Bagge-Hansen, Trevor M. Willey, Ke An, Yan Chen, Alex H. King, Scott K. McCall

correspondence to: mccall10@llnl.gov (SKM), rios@ornl.gov (ORR)

Aluminum alloys:

Table S1 lists the compositions of the standard commercial alloys shown in Fig. 1(a-b) of the main text.

Transmission Electron Microscopy:

The STEM HAADF Z-contrast images and EDS spectra were collected concurrently; this allowed identification of the intermetallic phases and quantify their composition. Fig. S1 illustrates the coherence across the Ce rich intermetallic-Al matrix phase boundary for an Al-8Ce-7Mg (wt. %) alloy. In both as-cast Al-12Ce-4Si-0.4Mg alloy and the material after heat-treatment, large (extending over many micrometers) intermetallics were observed where Ce concentration varied from ~20 at.% to ~55 at.% and as much as ~ 20 at.% of Si in the more Ce-rich precipitates. This suggests presence of $\text{Al}_{11}\text{Ce}_3$, Ce_5Si_3 , and the τ_1 phase: $\text{Ce}(\text{Al}_x\text{Si}_{1-x})_2$ in both materials. Due to close proximities of the K-edge energy for Mg (1.25 keV) and Al (1.48 keV), there was significant overlapping of Mg EDS peaks with the much larger Al peaks. As a result, the uncertainty of Mg concentration was higher (~0.2 at.%) than other elements with worse

detection limit (~ 0.5 at.%). Despite the low signal-to-noise ratio, Fig. S2 shows formation of thin, sharply cornered laths with higher Mg and Si concentration in the as-cast material surrounding the much larger Al-Ce intermetallic “core.” In contrast, these laths disappeared in the heat-treated material (Fig. S3) and the edges become rounded. Mg became more diffused in the bulk after heat treatment: concentration in the Al matrix increased from 1.0 ± 0.2 at.% to 1.5 ± 0.2 at.%. Si penetrated the intermetallic “cores”, and formed more $\text{Ce}(\text{Al}_x\text{Si}_{1-x})_2$ during heat treatment.

CALPHAD:

The ThermoCalc database includes a large collection of binary systems from which the phase diagrams presented in the main article Fig. 1(c-d) and here in the Supplementary Material (Figs. S4 and S5) were derived. The phase diagram for the Al-Ce-Si ternary system displayed in Fig. 3a of the article was calculated with the user-defined databases within ThermoCalc.

The format of the binary phase diagrams is designed to emphasize important characteristics: single phase regions, including the liquid, are shaded with blue; any multi-phase regions are shaded in orange; line compounds are labeled vertically on their corresponding composition; invariant reactions are marked with red lines.

SAXS/USAXS Analysis Overview:

In addition to the measurements of binary Al-Ce alloys described in the main manuscript, USAXS/SAXS measurements were performed at room temperature for two Al-Ce-based materials containing traditional Al-alloying elements (Si and Mg) in different concentrations. More specifically, USAXS/SAXS data were recorded for Al-12Ce-0.4Mg and Al-12Ce-4Si-0.4Mg (wt. %) alloys that had undergone T6 heat treatment, which are displayed in Figs. S6 and S7 respectively. The USAXS/SAXS data were collected on a combined Bonse-Hart/Pinhole SAXS/WAXS instrument at 9-ID-C at the Advanced Photon Source located at Argonne National Laboratory. All samples were prepared to varying thickness and exposed to a monochromatic X-ray beam of 24 keV for two minutes. With the sample thicknesses known, all data are calibrated and on an absolute scale. The shape I vs q within the USAXS/SAXS data depends on both the size distribution and shape of the dominant scattering phase. As such, modeling of this data provides a means of determining the shape and size dispersion of the intermetallics within the Al-12Ce-0.4Mg and Al-12Ce-4Si-0.4Mg alloys (wt. %).

The Porod plot (Fig. 3b) in the main article serves to show the dimensions of the intermetallic phases in the alloys. In this section, the intermetallic phases are characterized further by: (i) using the SEM imaging and USAXS data to determine whether the shape of the intermetallic phases, specifically whether they are best described by oblate or prolate ellipsoidal shapes, (ii) using this shape determination to extract the size distribution of large intermetallic phases, and (iii) remove the small angle scattering

from these larger phases to determine the approximate size of the very small unknown phases that are present.

Common approaches to determine the shape and/or size dispersion in SAXS are summarized below:

- (1) Model the phases as a specific shape and fit a size distribution.
- (2) Assume a size distribution and fit the shape.
- (3) Fit both the size distribution and the shape.

In cases (1) and (2) above, either the shape and or size distribution must be known before the other may be fit to the data. These two cases are necessary for materials containing broad size distributions of scatterers where no Bessel function oscillations are observed. Case (3) is applicable to only narrow size distributions or highly anisotropic particles, which is not the case for the intermetallic phases within the Al-Ce-based alloys and, therefore, (3) is not applicable in this study. Alternatively, analysis of the SEM images can provide enough information to determine both particle shape and size distribution. It is noted that this approach also verifies that the SEM imaging and USAXS are resolving the same phases. Two separate USAXS curves are simulated from the SEM imaging: one curve that assumes the intermetallic phases are rod-like, $I_{\text{rod}}(q)$, and another that assumes they are disk-like, $I_{\text{disk}}(q)$. The approximate shapes of the intermetallic phases are then indicated via the closest match between the simulated USAXS and the experimental USAXS. It is noted that the SEM data typically contains less statistical information than the volume-averaged USAXS data, which can lead to bias in the comparison and some error between the simulated and experimental USAXS.

Nevertheless, simulating the USAXS from SEM imaging is a useful exercise and can aid in the determination of particle shape. This approach is detailed below.

Evaluation of Particles with Dimensions Greater than 100nm

Based on SEM images (inset in Figs. S6 and S7) there is a size distribution of ellipsoidal particles, which are characterized by a radius (R), aspect ratio (AR), and some distribution $D(R)$. It is a well-known problem in small angle scattering (SAS) that a size distribution and moderate aspect ratios cannot be decoupled from the I vs q data.³⁴ For such cases, one requires additional information, which is provided by here via analysis of SEM images.

The limited range of an experimental sample probed by a series of SEM images limits the q -range that can be used for direct comparison with the USAXS data. The maximum q is determined from the minimum observable size, D_{minimum} , of features in the SEM image. The minimum resolvable size from the Al-12Ce-0.4Mg and Al-12Ce-4Si-0.4Mg samples correspond to maximum q values of: 0.007 \AA^{-1} and 0.003 \AA^{-1} , respectively, using the $2\pi/D_{\text{minimum}}$ approximation. The minimum q is more challenging to define. In principle, the maximum size (and therefore minimum q) should also be defined using features observed in the SEM images. Nonetheless, larger particles that might fit inside the image may not represent their total volume fraction in the sample and so the minimum q is taken to be 0.0001 \AA^{-1} for both alloys.

The discernment of particle shape begins with a particle analysis of the SEM images from each sample using the *ImageJ* software³⁴. This process involves the

application of macros for the following steps: grayscale conversion, spatial calibration, thresholding, and particle analysis. From the particle analysis macros, major (D_{maj}) and minor (D_{min}) dimensions of each particle were obtained. In the case that the imaged particles are rods, D_{min} is the radius and D_{maj} is the length, whereas for disks, D_{min} is the thickness and D_{maj} is the radius. These results are then used to simulate the USAXS scattering patterns, specifically the scattered intensity as a function of q for (i) prolate and (ii) oblate spheroids.

The scattered intensities from rods, $I_{rods}(q)$, and $I_{disks}(q)$ were calculated by the equations:

$$I_{rods}(q) = K \sum_{i=0}^{i=N} P \left(q, D_{min_i}, \frac{D_{maj_i}}{D_{min_i}} \right) \quad (1)$$

$$I_{disks}(q) = K \sum_{i=0}^{i=N} P \left(q, D_{maj_i}, \frac{D_{min_i}}{D_{maj_i}} \right) \quad (2)$$

$$P(q, R_i, A_R) = V^2(R, A_R) \int_0^1 F^2(q, R_{eff}(R, A_R, \alpha)) d\alpha \quad (3)$$

$$F(\mathbf{q}_R, R) = \left[\frac{3[\sin(qR) - qR \cos qR]}{[qR]^3} \right] \quad (4)$$

$$R_{eff}(R, A_R, \alpha) = R \sqrt{1 + \alpha^2 [A_R^2 - 1]} \quad (5)$$

where K is a scaling constant proportional to the contrast and number density in equations (1) and (2). To compare the simulated scattered intensity from equations (1) and (2) to the USAXS/SAXS data, $I_{rods}(q)$ and $I_{disks}(q)$ were slit smeared with the same

slit length as the experimental data. Quantitatively, the best model will yield the lowest χ^2 , by the equation:

$$\chi^2 = \left[\frac{I_{USAXS}(q) - I_{SEM}(q)}{E_{USAXS}(q)} \right]^2 \quad (6)$$

where $I_{SEM}(q)$ is either $I_{disk}(q)$ or $I_{rod}(q)$, χ^2 is minimized by changing the scaling factor, K , in equations (1) and (2) using the optimization function in Igor Pro. The results from each sample are shown in Figs S6 and S7 along with the resulting χ^2 obtained from Equation 6. In both cases, the value of χ^2 for disks is at least two orders of magnitude less than that obtained for rods. Therefore, the SEM/USAXS analysis strongly suggests that the phases observed by SEM have shapes that are closer to oblate ellipsoids rather than prolate ellipsoids. The aspect ratios and sizes for the particles observed by SEM imaging are tabulated in Table S2.

As mentioned previously, there are significant differences in statistical representation of the sample measured by USAXS and by SEM. If, for example, there is a large population of sphere-like particles ($AR=1$) with the rods, there would be better agreement between $I_{rods}(q)$ and the USAXS data. It is also important to note that the size range is limited in the SEM images that were used to simulate the small angle scattering. This can be improved with more images or by choosing images that represent the size and shape of the intermetallics. In this case, the simulated USAXS from each image can be combined using the relative magnification or optimally scaled. The relative scale was used in Fig.S7. These are just a few important considerations when choosing the appropriate images.

Assuming a value of AR , the size distribution, $D(R)$, of particles can be obtained via the method of maximum entropy³⁵ using the Irena package for Igor Pro³⁶. In this method, the scattered intensity is calculated the equation:

$$I(q) = [\Delta\rho]^2 \sum_i \frac{P(q, R_i, A_R)}{V(R_i, A_R)} D(R_i) \Delta R_i \quad (7)$$

where the contrast, $[\Delta\rho]^2$, is set to $84.5 \times 10^{20} \text{ cm}^{-4}$, which is the theoretical value for a particle of $\text{Al}_{11}\text{Ce}_3$ surrounded by an Al matrix. Deviations from this value will scale $D(R)$, which can be used to obtain the number density of scatterers, N , that have radii in each bin ΔR_i . The method of maximum entropy provides the best-fit function, $D(R)$, assuming the mean aspect ratio obtained from SEM imaging (Table S2). The resulting model fits to the USAXS data and size distributions, $D(R)$ are shown in Fig. S8. The misfits at very low- q can be attributed to intermetallics that are too large to resolve with USAXS ($> 6 \mu\text{m}$) or have aspect ratios closer to 1.

Evaluation of Particles with Dimensions Less than 100nm

A smaller population is present in both evaluated samples. Similar to the lower q region, the USAXS data contains a very broad Guinier knee, which can be again attributed to a system of either disk or rod-like particles. Because of the size-dispersity, unknown aspect ratio, AR , and composition these data cannot be reliably modeled. Instead, only rough dimensions of these phases are extracted from the high- q portion of the USAXS data by first subtracting the scattering from larger particles obtained by the method of maximum entropy. After this subtraction, there is a scattering intensity in the q

region: $0.02 \text{ \AA}^{-1} < q < 0.1 \text{ \AA}^{-1}$. Based on the $2\pi/q$ approximation, this scattering is from phases with dimensions between 6 nm and 30 nm.

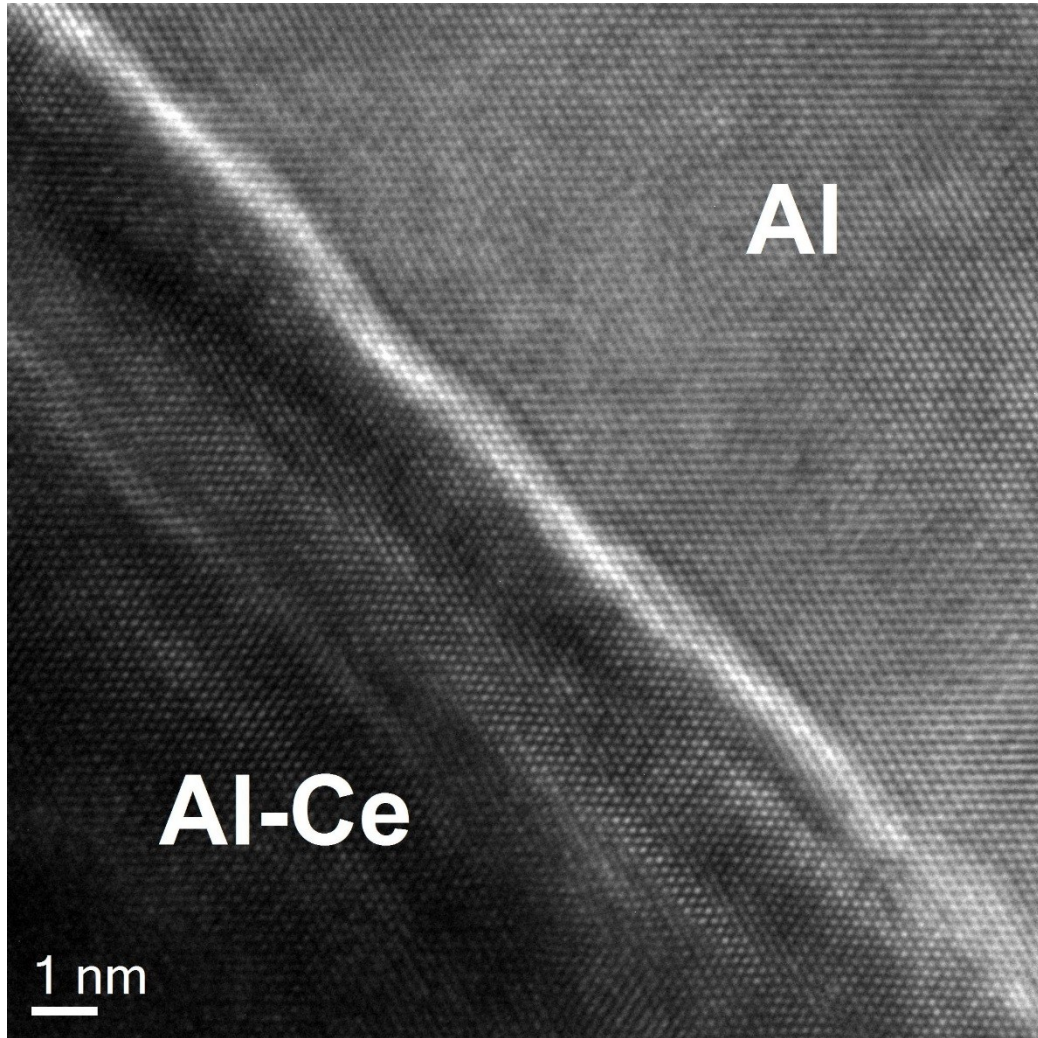


Fig. S1: TEM image illustrating coherence across the intermetallic-Al phase boundary in a new Al-8Ce-7Mg (wt. %) sample. The lower left portion of the image is darker due to the presence of the much higher Z Ce atoms which attenuate electron transmission more strongly than Al.

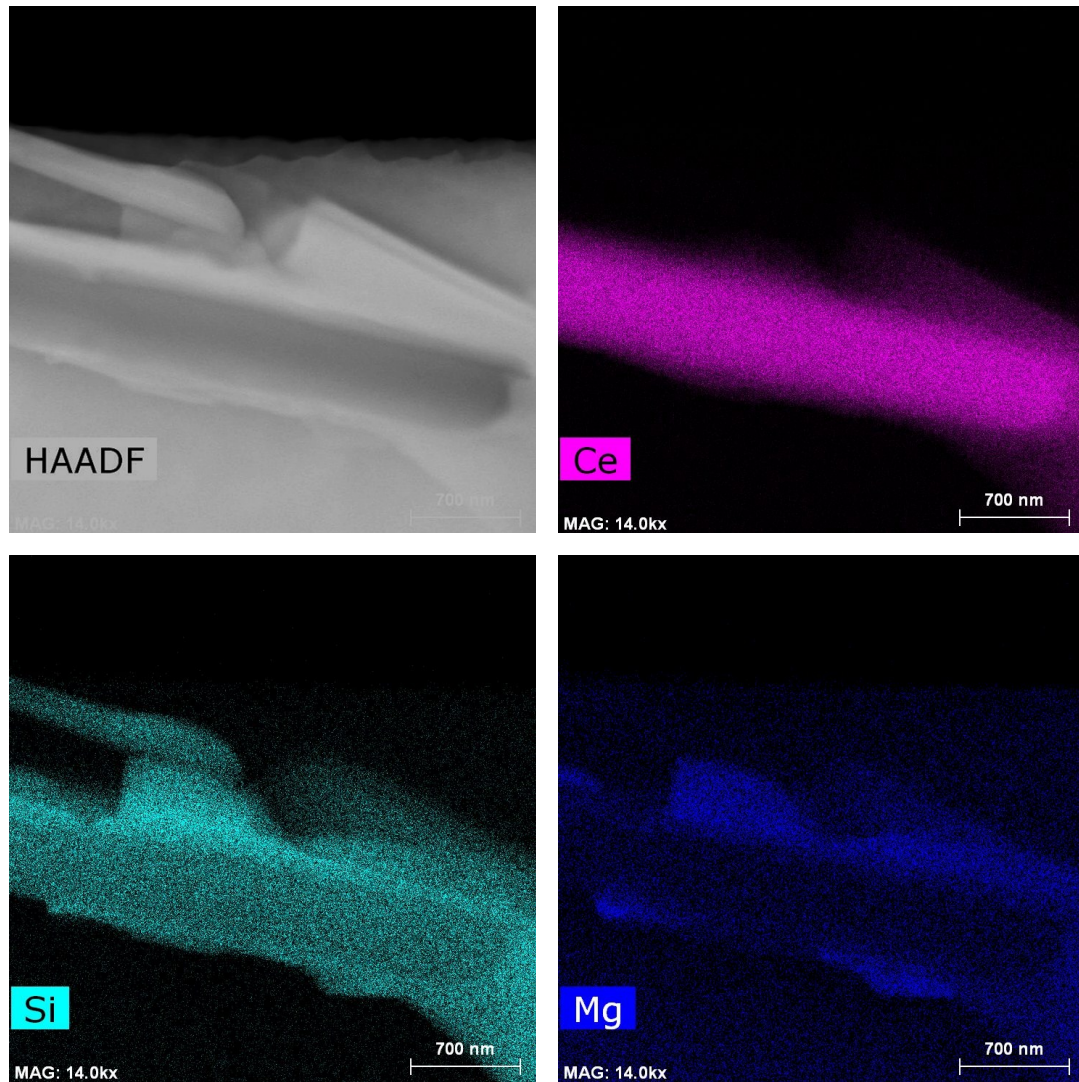


Fig. S2: Intermetallic formed from Al-8Ce-4Si-0.4Mg (wt%) in the as cast condition (Al not shown for clarity). The Ce component forms a core in the feature, which is surrounded by Si and Mg. While the magnesium signal is diffuse, there is a richer region consistent with high Si and lower Ce content on these images.

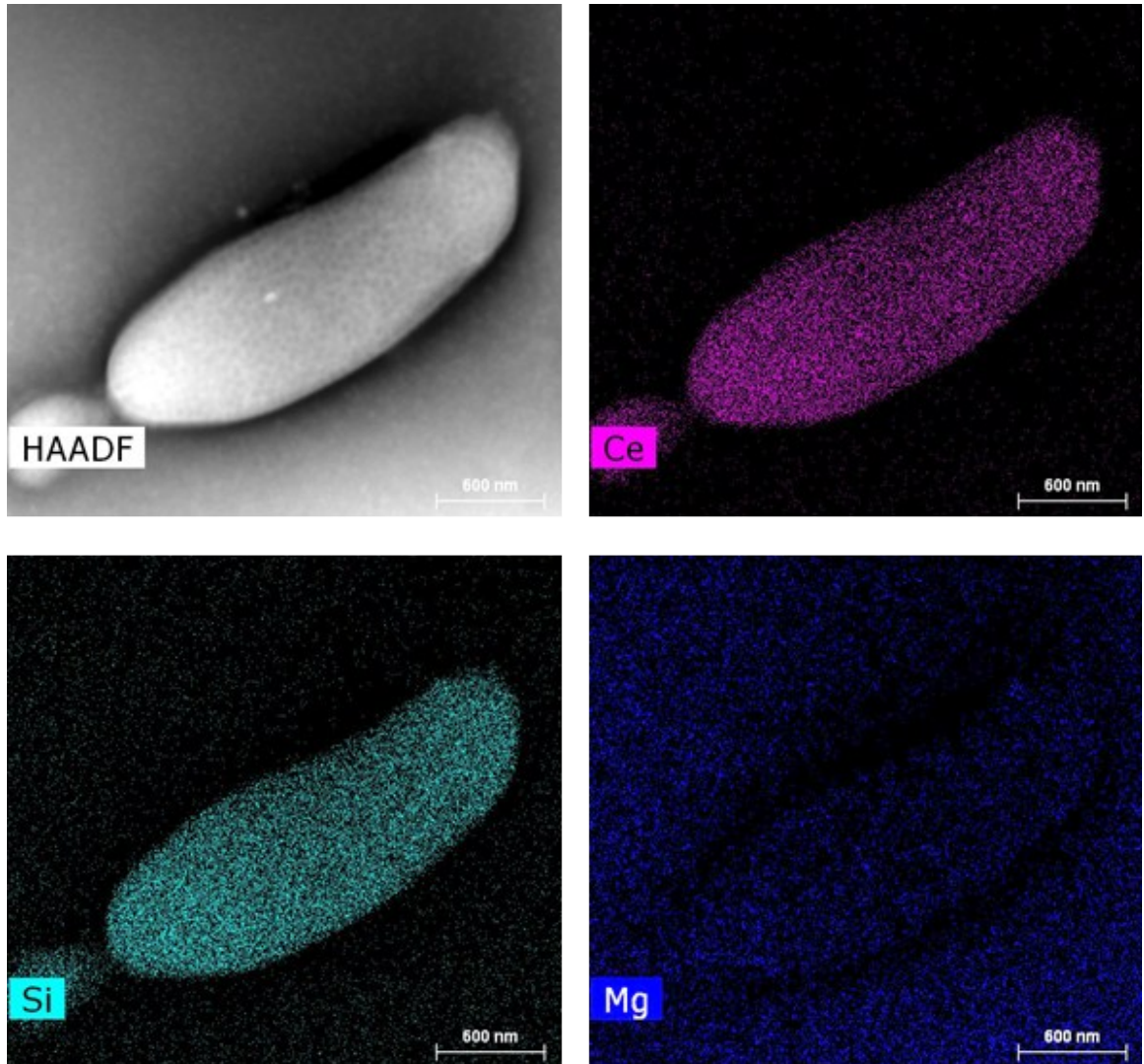


Fig. S3: Intermetallic in a sample of Al-8Ce-4Si-0.4Mg (wt. %) after undergoing a T6 heat treatment (540 °C for 10 hours). The magnesium signal contrast has been increased relative to Fig. S4 to show it is uniformly distributed and comparable to the noise. The result suggests it has diffused more uniformly throughout the sample when compared to the as cast condition of Fig. S4. The shape of the inclusion has also rounded, reducing the surface energy.

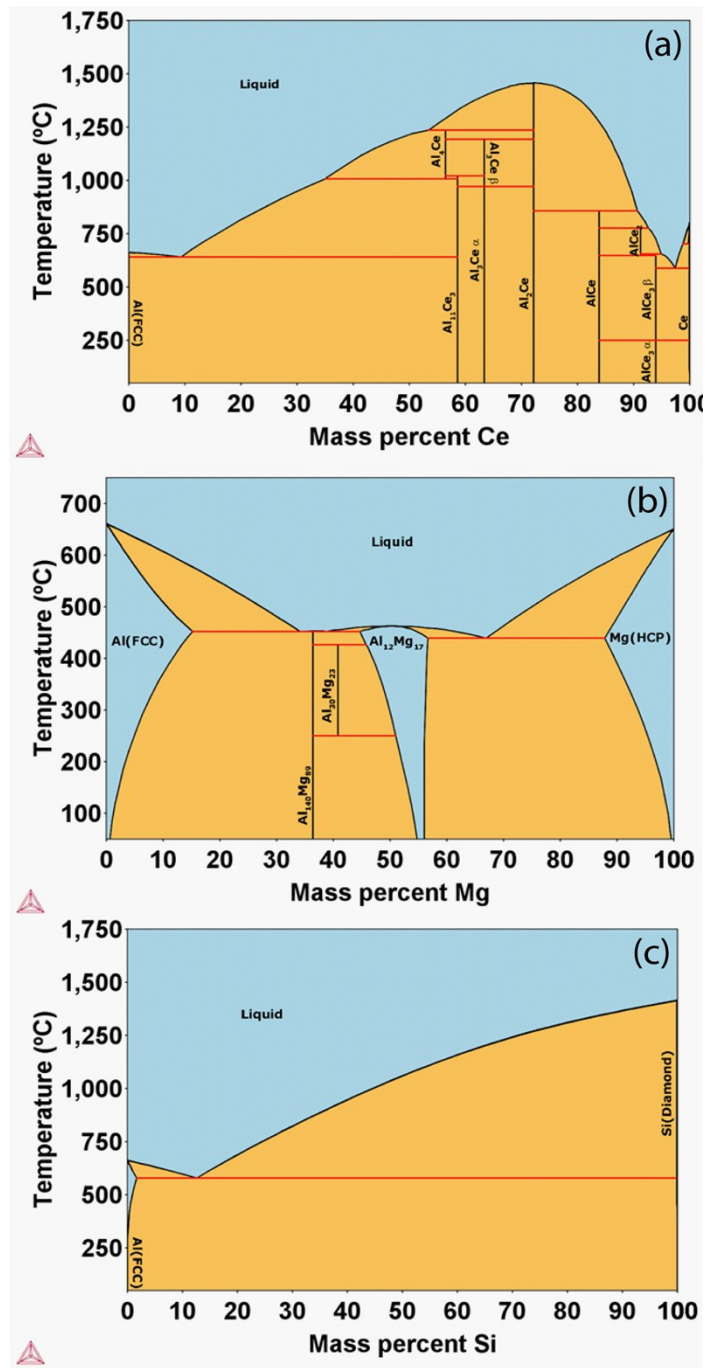


Fig. S4: Full binary phase diagrams thermodynamically assessed using the CALPHAD method in combination with ThermoCalc software for aluminum alloyed with (a) cerium, (b) magnesium, and (c) silicon

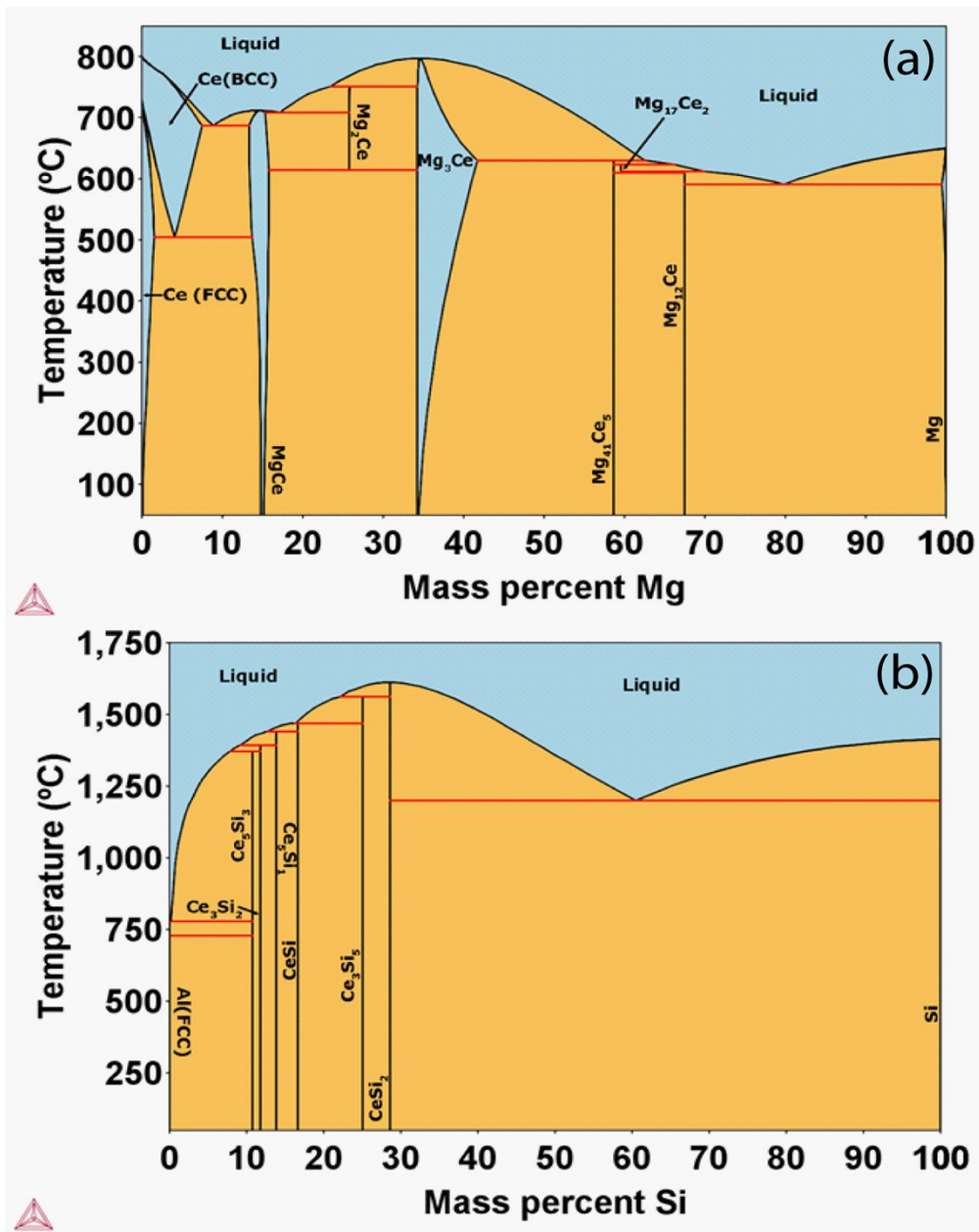


Fig. S2: Full binary phase diagrams thermodynamically assessed using the CALPHAD method in combination with ThermoCalc software for cerium alloyed with (a) magnesium, and (b) silicon.

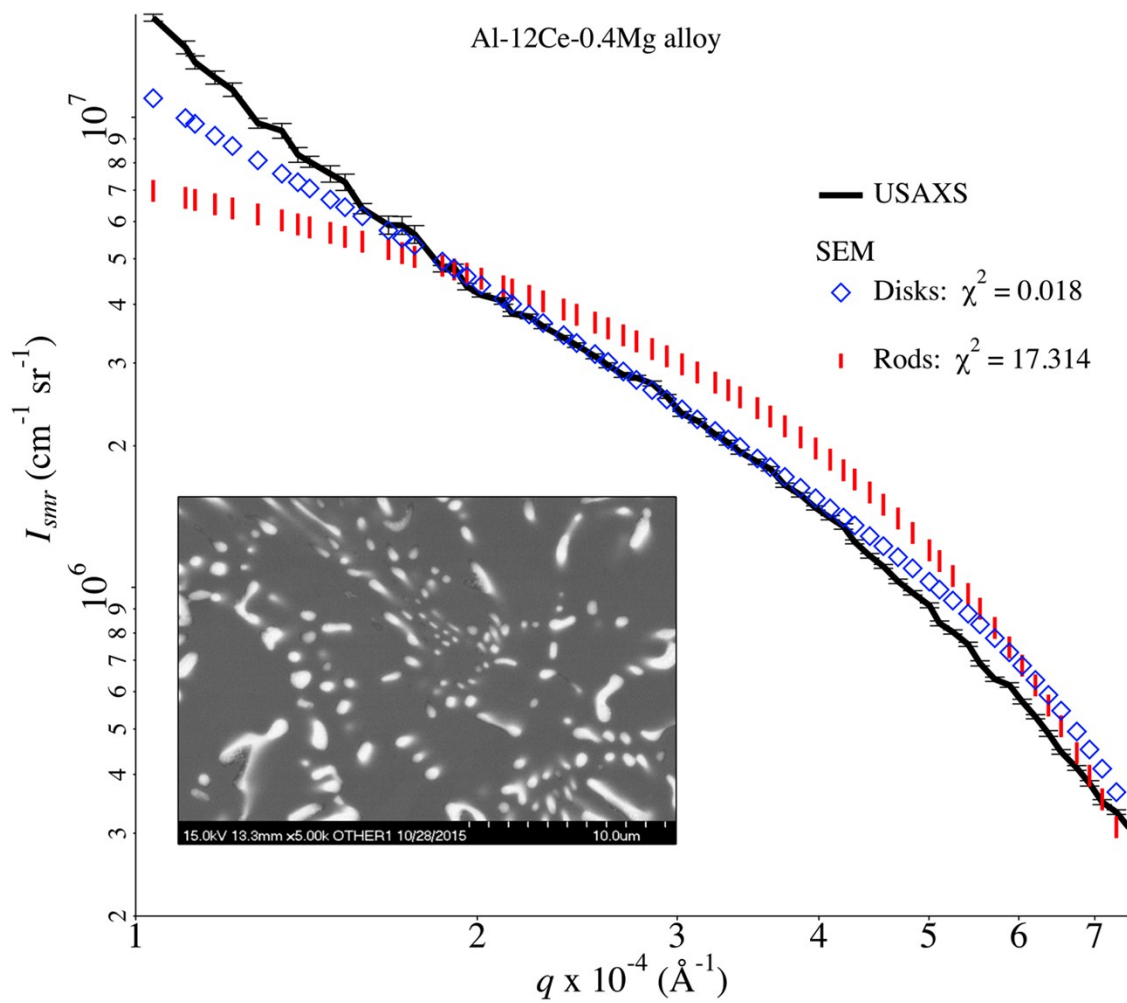


Fig. S6: A log-log comparison of experimental USAXS/SAXS data recorded for the Al-12Ce-0.4Mg alloy (black line) and versus simulated data generated assuming rod-like (red vertical lines) and disc-like (blue diamonds) phases. Inset: A representative SEM image of the Al-12Ce-0.4Mg (wt. %) alloy.

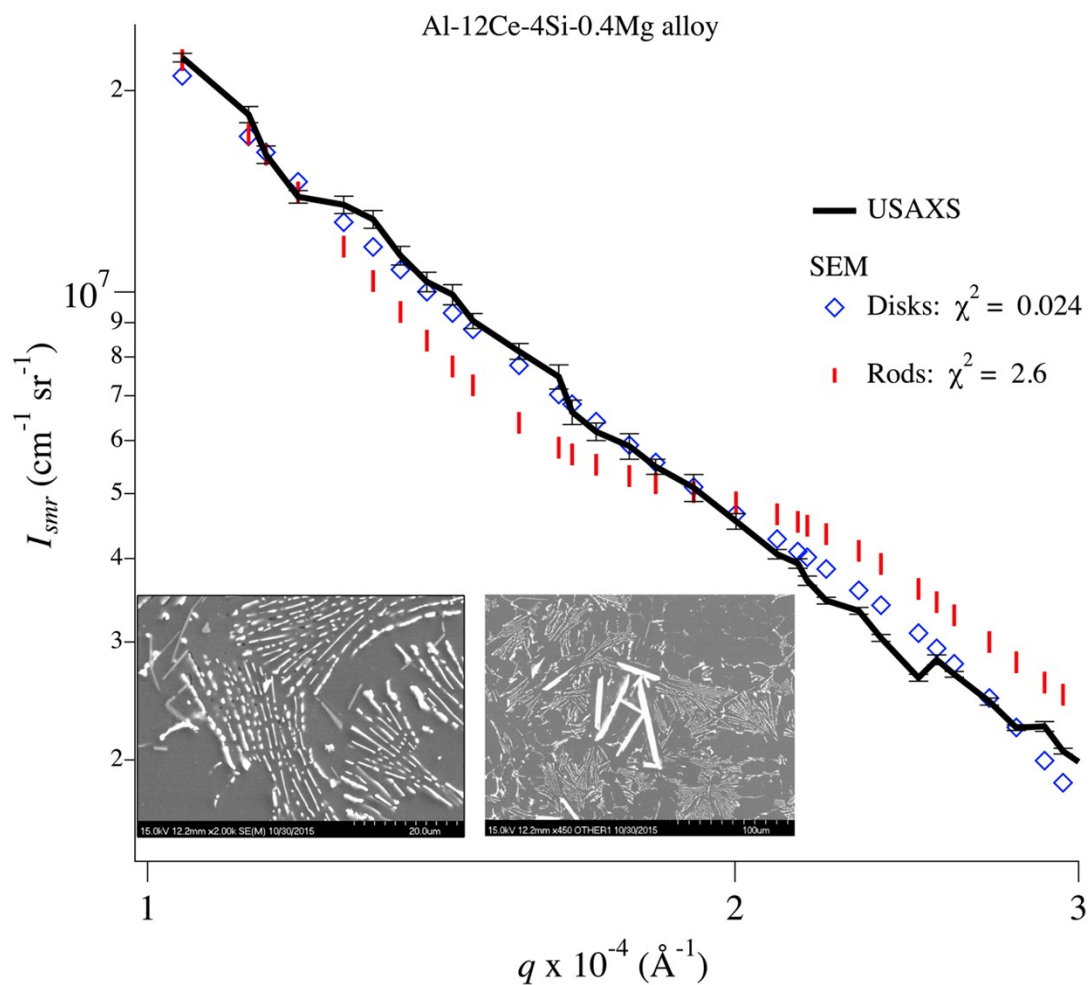


Fig. S7: A log-log comparison of experimental USAXS/SAXS data recorded for the Al-12Ce-4Si-0.4Mg (wt. %) alloy (black line) and versus simulated data generated assuming rod-like (red vertical lines) and disc-like (blue diamonds) phases. Inset: Two representative SEM images of the Al-12Ce-4Si-0.4Mg (wt. %) alloy.

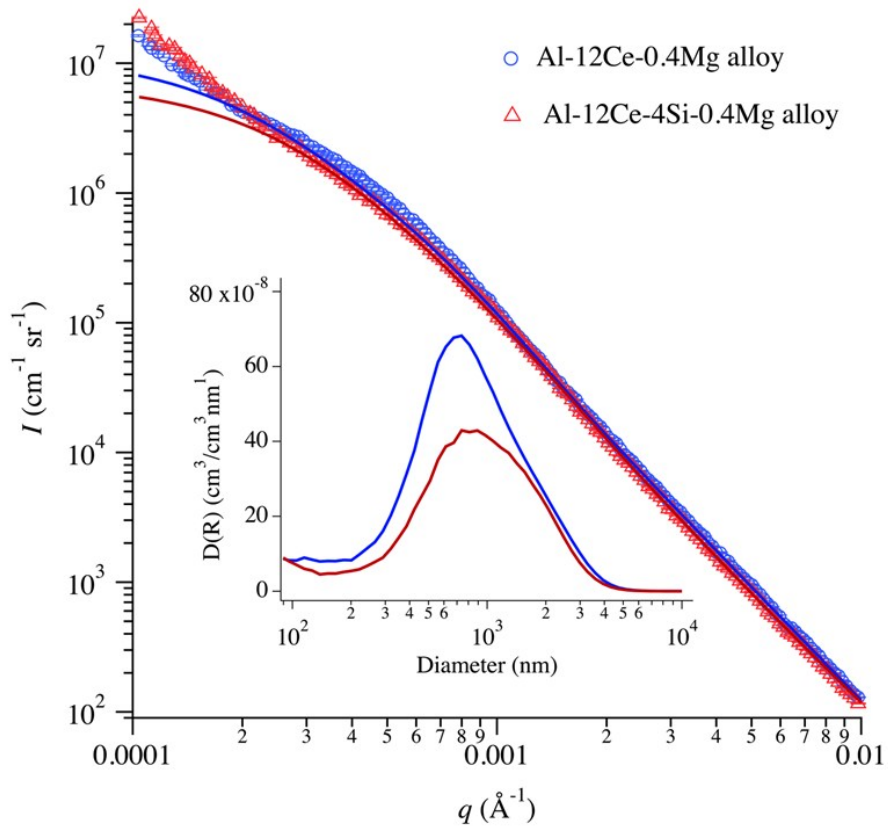


Fig. S8: A log-log plot of the USAXS data (markers) collected from the Al-12Ce-0.4Mg (wt. %) alloy (blue) and the Al-12Ce-4Si-0.4Mg (wt. %) alloy (red). The model intensities from the method of maximum entropy are shown as solid lines. The number distributions for each data set are shown in the inset. In each case, most phases are larger than 100 nm.

Table S1:

Maximum compositions of common commercial aluminum alloys by weight percent (balance is aluminum) unless a range is given.

| Alloy | Si | Fe | Cu | Mn | Mg | Zn | Ti |
|---------------|-----------|-----------|-----------|-----------|-----------|-----------|-----------|
| 201 | 0.10 | 0.15 | 4.0-5.2 | 0.2-0.5 | 0.15-0.55 | 0.10 | 0.15-0.35 |
| 206 | 0.10 | 0.15 | 4.2-5.0 | 0.20-0.50 | 0.15-0.35 | 0.10 | 0.15-0.30 |
| 224 | 0.06 | 0.10 | 4.5-5.5 | 0.2-0.5 | -- | -- | 0.35 |
| 240 | 0.50 | 0.50 | 7.0-9.0 | 0.3-0.7 | 5.5-6.5 | 0.10 | 0.20 |
| 242 | 0.70 | 1.00 | 3.5-4.5 | 0.35 | 1.2-1.8 | 0.35 | 0.25 |
| 295 | 0.7-1.5 | 1.00 | 4.0-5.0 | 0.35 | 0.03 | 0.35 | 0.25 |
| A319.0 | 5.5-6.5 | 1.00 | 3.0-4.0 | 0.50 | 0.10 | 3.00 | 0.25 |
| 336 | 11.0-13.0 | 1.20 | 0.5-1.5 | 0.35 | 0.7-1.3 | 0.35 | 0.25 |
| 355 | 4.5-5.5 | 0.60 | 1.0-1.5 | 0.50 | 0.4-0.6 | 0.35 | 0.25 |
| 356 | 6.5-7.5 | 0.60 | 0.25 | 0.35 | 0.2-0.45 | 0.35 | 0.25 |
| 413 | 11.0-13.0 | 2.00 | 1.00 | 0.35 | 0.10 | 0.50 | -- |
| 514 | 0.35 | 0.50 | 0.15 | 0.35 | 3.5-4.5 | 0.15 | 0.15 |
| 518 | 0.35 | 1.80 | 0.25 | 0.35 | 7.5-8.5 | 0.15 | -- |
| 535 | 0.15 | 0.15 | 0.05 | 0.10-0.25 | 6.2-7.5 | -- | 0.10-0.25 |

Table S2:

The mean radius and aspect ratio obtained from the SEM/USAXS analysis. The standard deviation, σ , for each of these values was obtained from the particle size analysis of the SEM imaging of the Al-12Ce-0.4Mg and Al-12Ce-4Si-0.4Mg (wt. %) alloys

| | R_{disk} | σ | A_R | σ |
|-------------------|------------|----------|-------|----------|
| Al-12Ce-0.4Mg | 927 nm | 732 nm | 0.6 | 0.20 |
| Al-12Ce-4Si-0.4Mg | 2280 nm | 2189 nm | 0.4 | 0.23 |

Supplemental References

34. C. A. Schneider, W. S. Rasband and K. W. Eliceiri, *Nat Meth*, 2012, **9**, 671-675.
35. J. A. Potton, G. J. Daniell and B. D. Rainford, *J. Appl. Crystallogr.*, 1988, **21**, 663-668.
36. J. Ilavsky and P. R. Jemian, *J. Appl. Crystallogr.*, 2009, **42**, 347-353.